Journal of
Materials Chemistry C

ROYAL SOCIETY
OF CHEMISTRY

PAPER

View Article Online
View Journal | View Issue

Cite this: *J. Mater. Chem. C*, 2020, **8**, 2798

Realizing graphene-like Dirac cones in triangular boron sheets by chemical functionalization†

Shao-Gang Xu,[a] Zhong-Jia Chen,[bc] Yu-Jun Zhao,[b] Xiuwen Zhang,*[a] Hu Xu*[c] and Xiao-Bao Yang*[b]

Received 26th November 2019,
Accepted 14th January 2020

DOI: 10.1039/c9tc06464h

rsc.li/materials-c

The most important feature in graphene is its unique Dirac cone, which is closely associated with many novel properties. However, this type of Dirac cone is rare and difficult to realize in non-group-IV two-dimensional (2D) materials. In this work, we have theoretically designed a family of triangular B_3X (X = H, F, and Cl) monolayers with graphene-like Dirac cones in terms of constituent atomic orbitals and high thermal stability. Furthermore, based on the idea of effective charge transfer, we have uncovered the key mechanism for the realization of graphene-like Dirac cones with a concise bond distribution model, which is valid for the 2D boron-based materials with a single Dirac cone and double Dirac cones. Our results offer new insights into the design of 2D boron-based Dirac semimetals by chemical adsorption, which may stimulate the development of 2D boron research.

1. Introduction

The discovery of new physical properties and applications in graphene has stimulated a rush of attention on two-dimensional (2D) materials.[1] Most of the novel properties of graphene are due to the unique linear-dispersion Dirac cone, including the Klein tunneling, high carrier mobility, half-integer quantum Hall effects, *etc.*[2–4] However, 2D Dirac materials are relatively rare compared with the numerous 2D materials, which is due to the rigorous requirements on the symmetry, parameters, Fermi level, and band overlap of 2D materials for achieving Dirac cones.[5] Thus, the most common Dirac materials are found in the group-IV honeycomb structures (graphene, silicene and germanene)[6,7] and several graphynes (sp–sp^2 carbon allotropes),[8,9] and the search for other 2D Dirac systems is very urgent.

Boron, situated next to carbon in the periodic table, is one of the most fascinating elements because of its complicated chemistry and flexible bonding patterns.[10] After the triumph of boron clusters in experiments,[11] the long-sought 2D boron sheets have been recently synthesized on metal substrates.[12,13] As is well known, the polymorphic boron sheets exhibit a variety of properties, including mechanical compliance, optical transparency, superconductivity and semiconductivity.[14,15] Furthermore, novel topological fermions may emerge in the boron sheets with special lattice structures. Until now, the Dirac fermions and nodal-line fermions have been reported in the β_{12} and hs-s B phases,[16–19] whereas these materials are intrinsically metallic and the band crossing points in these structures are away from the Fermi level.

Indeed, due to the special electron deficiency of boron, the ideal Dirac cones can not be realized in pure boron sheets, whereas the strategy of surface chemical functionalization may help to obtain the Dirac states. Based on the idea of charge transfer, the approach of embedding a suitable metal atom at the vacancy of the honeycomb boron sheet may be very effective, such as in BeB_2, FeB_2, TiB_2, and ZrB_2 monolayers.[20–23] Since the single 2p electron in boron could behave both ionically and covalently,[24] the covalent bonds can induce the optimal orbital filling for the Dirac states, like the bilayer boron (*P*6/*mmm*) and B_6O sandwich.[25,26] However, the experimentally observed 2D B is mainly based on triangular B structures.[12,27] It is not clear whether the (honeycomb) graphene-like Dirac cones can be realized in triangular B sheets.

In this work, based on the comprehensive bond distribution model and first-principles calculations, we have proposed a family of stable 2D B_3X (X = H, F, and Cl) monolayers based on a triangular B framework under H (or F, Cl) functionalization hosting the graphene-like Dirac cones. Combined with the results of charge transfer and model analysis, we have offered new insight into the origin of the Dirac cones, which is general for the Dirac materials with different adsorption ligands. In addition, the newly predicted phases have been proved to

---

[a] *Shenzhen Key Laboratory of Flexible Memory Materials and Devices, Key Laboratory of Optoelectronic Devices and Systems of Ministry of Education and Guangdong Province, College of Physics and Optoelectronic Engineering, Shenzhen University, Shenzhen 518060, P. R. China. E-mail: xiuwenzhang@szu.edu.cn*

[b] *Department of Physics, South China University of Technology, Guangzhou 510640, P. R. China. E-mail: scxbyang@scut.edu.cn*

[c] *Department of Physics, Southern University of Science and Technology, Shenzhen 518055, P. R. China. E-mail: xuh@sustech.edu.cn*

† Electronic supplementary information (ESI) available. See DOI: 10.1039/c9tc06464h

have excellent dynamic and thermal stabilities, implying their experimental feasibility, which may be used as a practical platform to design high-performance electronic devices.

2. Computational methods

All the density functional theory (DFT) calculations were carried out by using the Vienna *ab initio* simulation package (VASP),[28] and the electron-ion interactions were described by the projector augmented wave (PAW) potentials.[29] The Perdew–Burke–Ernzerhof (PBE) functional within the generalized-gradient approximation (GGA) framework was adopted to treat the exchange–correlation interaction of electrons.[30] All the initial lattice constants and atomic positions were fully relaxed until the forces on each atom were smaller than -0.01 eV Å^{-1}. The energy cutoff of the plane-wave basis sets was 480 eV. In all calculations, a vacuum region of 21 Å along the z direction was added to the model to avoid interaction between adjacent images. To investigate the dynamic and thermal stability, we calculated the phonon band structures by using a supercell approach as implemented in the PHONOPY program[31] and carried out *ab initio* molecular dynamics (AIMD) simulations with a Nosé heat bath scheme at given temperature.[32]

3. Results and discussion

The bond distribution model for previously attempted H functionalized B sheets

We consider the bond distribution model by using the ideal Dirac cones in group-IV honeycomb structures[5] as the starting point. Because of the electron deficiency of boron, the honeycomb structures can not be realized in freestanding 2D boron.[33–36] In theory, when exactly doping 1 e per atom, the honeycomb borophene becomes isoelectronic to graphene and the Dirac point shifts to the Fermi level.[37] It was expected that hydrogenation may act as an effective strategy, where a single hydrogen atom can share its electron with the boron atom, and thus the B–H system is isoelectronic with carbon.[38] However, in the hydrogenated monolayer honeycomb boron, the expected Dirac cones are missing.[39] This failure of realizing graphene-like Dirac cones in the honeycomb B–H sheets is due to the plausible electron compensation strategy that ignores the complicated bonding patterns between boron atoms. For example, the three-center two-electron (3c-2e) bonding was initially proposed to explain the electron configurations in diborane (see Fig. 1d),[40] and the 8-electron rule was applied to understand the distribution of hexagonal vacancies in the magic boron clusters and stable boron sheets.[41–43] The experimental honeycomb hydrogen boride sheet B_2H_2 (*Cmmm*)[39,44] can be well understood by the 8-electron bond distribution model (see Fig. 1d), which is constructed by 2 B–H–B 3c-2e and 2 B–B 2c-2e bonds in the unit cell, implying that the B–H–B bridged 3c-2e bond is the key structural unit. The hydrogen atom in the honeycomb B_2H_2 sheet is shared by two B atoms (Fig. 1d), which explains the failure of the assumed isoelectronic character of carbon. The previously considered hydrogenated triangular boron sheet, 2D borane (*Pmmn*), possesses two symmetry-related Dirac cones meeting right at the Fermi level,[45] which are, however, totally different from the counterpart in graphene. As shown in Fig. 1(a–c), the orbital-resolved band structures demonstrate that the Dirac-cone in 2D borane is dominated by the in-plane p_x and p_y orbitals of B atoms, which are different from the out-of-plane p_z orbitals in graphene, as the honeycomb-like atomic arrangements (graphene-like) are missing in 2D borane.

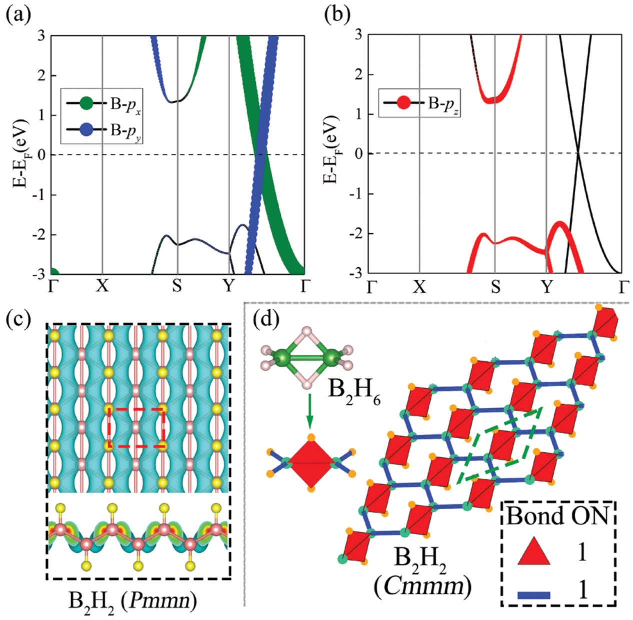

Fig. 1 (a and b) The projected band structures of triangular B_2H_2 (*Pmmn*); the meaning of dots with different colors is shown in the inset (E_F is set to 0). (c) The band decomposed charge density of triangular B_2H_2 (*Pmmn*) at the Dirac point. (d) Bond model analysis for the diborane and B_2H_2 (*Cmmm*) monolayer; the occupation number (ON) of the 2c-2e and 3c-2e bonds is listed on the right side. The red triangle represents the 3c-2e B–H–B bond and the blue line indicates the 2c-2e B–H bond in B_2H_6 (with two 3c-2e B–H–B bonds involving the bridging hydrogen atoms and four 2c-2e B–H bonds) or 2c-2e B–B bond in honeycomb B_2H_2.

Designing H (F and Cl) functionalized triangular B sheets to realize graphene-like Dirac cones

From the analysis of the average electron compensation (AEC) mechanism,[43] it is clear that there is one excess e per $p(\sqrt{3} \times \sqrt{3})$ triangular boron sheet. If the excess e in the above triangular boron sheet can be effectively transferred, the left 3 boron atoms possess an 8-electron bond distribution. We can use the H functionalization to accept this excess e from B, analogously to F or Cl functionalization, but different from the previous H functionalization on B sheets (Fig. 1), where H prefers to donate an electron. For certain arrangements of functionalized B sites, a honeycomb B structure is left without functionalization (see Fig. 2), in which the honeycomb atomic arrangements could enable the graphene-like Dirac cones. Based on the above analysis, we have designed several adsorption

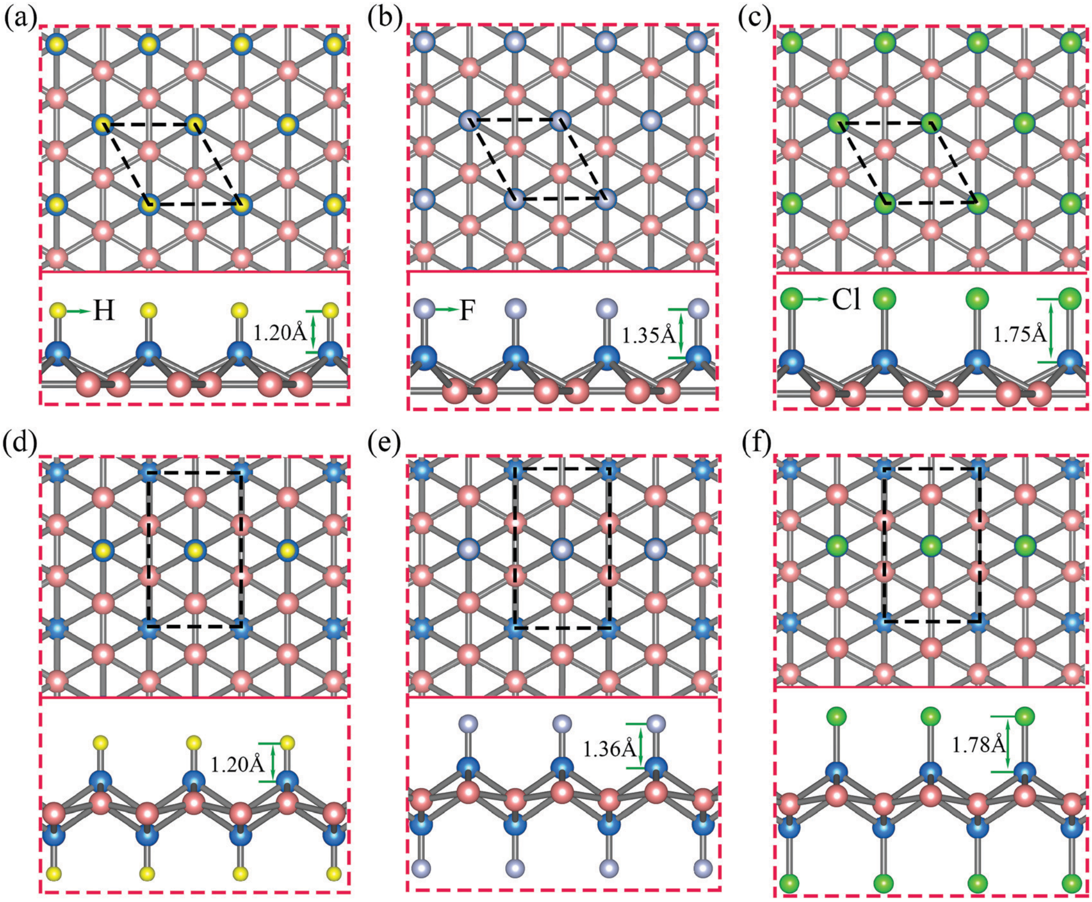

Fig. 2 Atomic structures of the newly predicted B–X (X = H, F, and Cl) phases. (a–c) Represent the structures of B_3X monolayers. (d–f) Represent the structures of B_6X_2 monolayers. The blue atoms represent the B atoms at the adsorption sites. The black dashed lines represent the unit cell of the corresponding 2D structures.

configurations to verify the ideas. As shown in Fig. 2(a), the hydrogen atom is absorbed on the top of the B atom, and the B–H bond length is 1.20 Å. Similarly, the single-side halogenated B sheets were also tested, and the B–X (X = F and Cl) bond is longer than the B–H bond (see Fig. 2(b and c)). Considering the possible electrostatic repulsion interactions, we have performed the study of double-side hydrogenated/halogenated structures, and where the non-adsorption B plane is slightly distorted. As shown in Table S1 (ESI†), all the double-side systems are more stable than the single-side ones. Since the hydrogen boride sheets (B_2H_2/*Cmmm*) have been derived from MgB_2 by cation exchange,[44] our predicted B–H structures may be produced due to the relatively lower formation enthalpy (see Table S2, ESI†). Furthermore, the phonon dispersions along the high-symmetry lines and AIMD snapshots at a higher temperature indicate that the new B–H phases have outstanding dynamic and thermal stabilities (see Fig. S1 and S2, ESI†). In addition, the lowest, out-of-plane, acoustic phonon branch (ZA mode) has a purely quadratic relationship near the zone center (see Fig. S1, ESI†), which is a solid general rule in layered materials.[46,47] Notably, the stability of the single-side and double-side functionalized B_3X can be well understood by the 8-electron bond distribution model based on 3c-2e bonds with the occupation number of 2/3 (see Fig. 5c).

For the single-side B_3X (X = H, F, Cl) monolayers, the band structures show a similar Dirac cone located at the Fermi level (see Fig. 3a–c), and the band structures of the stable double-side B_6X_2 (X = H, F, Cl) configurations also exhibit the desired Dirac cones (see Fig. 3d–f). The corresponding Fermi velocities were obtained by using the expression $\nu_f = \partial E/\hbar\partial k$, and the calculated ν_f values for the Dirac materials are shown in Table S1 (ESI†), which are comparable to that of graphene ($\nu_f = 0.82 \times 10^6$ m s^{-1}).[38] In order to explore the origin of the Dirac cone, the orbitally resolved band structures for the above phases are presented in Fig. 4 and Fig. S3 (ESI†). Clearly, all the Dirac cones are dominated by the out-of-plane p_z orbitals of B atoms, which can be confirmed by the band decomposed charge density at the Dirac point. The charge density distribution is derived from the honeycomb B planes, which indicates that the B atoms in this plane play the role of C atoms in graphene. In addition, we have studied the models of single-side B_3X with 3 and 4 times supercells, as shown in Fig. S5 (ESI†). Clearly, the results of B_3X show similar Dirac cones like the counterparts in the graphene supercells. Especially, the $p(2 \times 2)$ B_3X supercells exhibit the typical Dirac cones at the *K* point (see Fig. S5(f–h), ESI†), which indicated

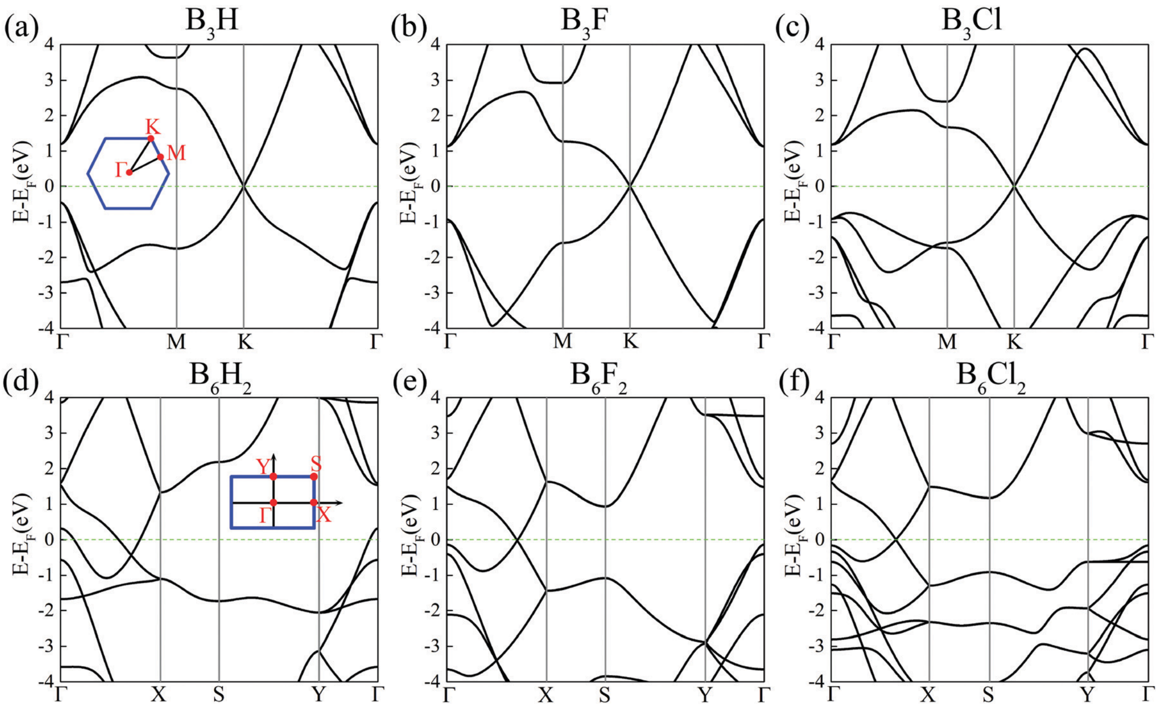

Fig. 3 Band structures of the newly predicted B–X (X = H, F, and Cl) phases. (a–c) Represent the band structures of B_3X monolayers. (d–f) Represent the band structures of B_6X_2 monolayers. (E_F is set to 0). All the data in this figure were calculated using the PBE functional.

that the graphene electronic properties can be realized in these B_3X adsorption systems.

Compared with the metallic triangular boron sheets,[33] the Dirac cones in the above systems are attributed to the chemical functionalization of X, and insight into the electronic bonding may be very helpful. Here, we divided the 2D systems into three parts: (i) X is the adsorbed element (X = H, F, and Cl); (ii) B1 represents the B atoms bonded with X; (iii) B2 represents the B atoms of the honeycomb planes. As shown in Fig. 5a, the bonding and antibonding states near the Fermi level of the (B1 + X) parts are smaller than the counterparts of B2, which indicated that the strong bonding interactions between X and B1 lead to the repulsion of the corresponding bonding and antibonding states. Clearly, the electronic states near the Fermi level are dominated by the honeycomb B2, which is in accord with the band decomposed information in Fig. 4. Here, the choice of X is motivated by transferring the excess electrons in triangular B sheets. As shown in Fig. 5b, the Bader charge analysis indicated about 1 e transfer from B1 to X, and the large charge transfer demonstrated the ionic nature of the B1–X bond. Furthermore, the above charge transfer processes ensure that the B atoms of the B2 layer share similar charge distributions (3.16–3.22). The electron localization function (ELF) images also reveal the graphene-like bonding features of the B2 layer, as the surplus electrons have been transferred to X (see Fig. S4, ESI†).

Effective Hamiltonian for the graphene-like Dirac cones in the functionalized triangular B sheet

Due to the strong electronegativity of halogens, ideal Dirac cones have been realized in the B_3X/B_6X_2 (X = F and Cl) systems. In order to investigate the Dirac cone, we have constructed a six band tight-binding (TB) model for the typical B_6F_2 by choosing the p_z orbitals of all the B atoms as the basis. When the spin–orbit coupling (SOC) effect is ignored, the effective Hamiltonian can be written as

$$H_{\mathrm{TB}} = \begin{bmatrix} \varepsilon_a & t_2u^* & t_2u & t_4v & 0 & t_4v^* \\ t_2u & \varepsilon_b & t_1u^* & t_3v^* & t_4v & 0 \\ t_2u^* & t_1u & \varepsilon_c & 0 & t_4v^* & t_3v \\ t_4v^* & t_3v & 0 & \varepsilon_d & t_2u^* & t_1u \\ 0 & t_4v^* & t_4v & t_2u & \varepsilon_e & t_2u^* \\ t_4v & 0 & t_3v^* & t_1u^* & t_2u & \varepsilon_f \end{bmatrix},$$

where

$$u = e^{i2\pi k_2/3},\ v = 2e^{i\pi k_2/3}\cos(\pi k_1).$$

Here, k_1 and k_2 are direct coordinates in the Brillouin zone. The on-site energies ε_i (i = a, b, c, d, e, f) of the six occupied sites are given by

$$\vec{R}_a = (0,0),\quad \vec{R}_b = a_0\left(0, \frac{2\sqrt{3}}{3}\right),\quad \vec{R}_c = a_0\left(0, \frac{\sqrt{3}}{3}\right),$$

$$\vec{R}_d = a_0\left(\frac{1}{2}, \frac{5\sqrt{3}}{6}\right),\quad \vec{R}_e = a_0\left(\frac{1}{2}, \frac{\sqrt{3}}{2}\right),\quad \vec{R}_f = a_0\left(\frac{1}{2}, \frac{\sqrt{3}}{6}\right),$$

where a_0 is the lattice constant of B_6F_2. The transfer energies t_i (i = 1, 2, 3, 4) represent four unequivalent pairs between the

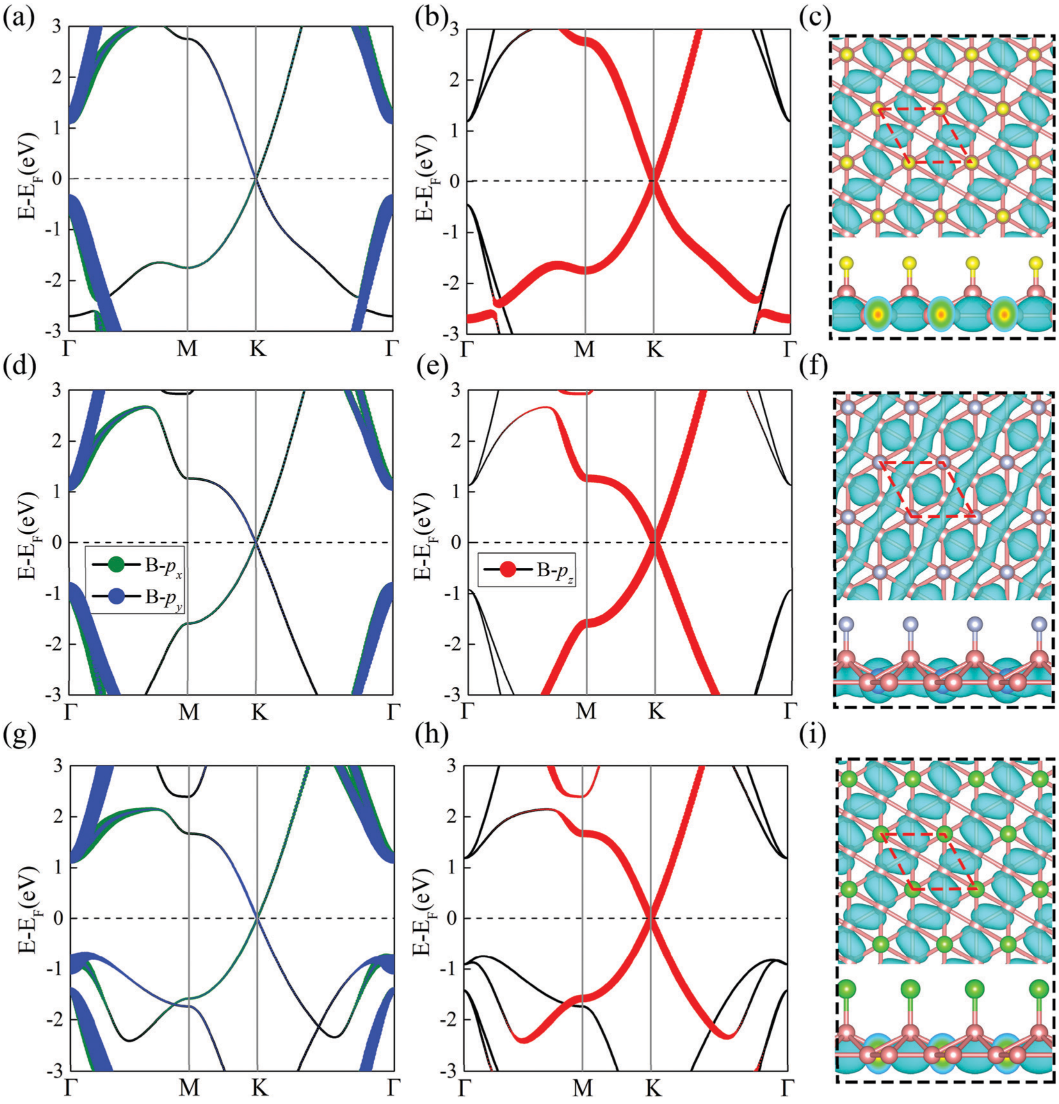

Fig. 4 Orbital-resolved band structures and band decomposed charge density of the new phases. (a–c, d–f, and g–i) represent the projected band structures and band decomposed charge density at the Dirac point of B_3X (X = H, F, and Cl) monolayer, respectively. All the data in this figure were calculated using the PBE functional.

nearest neighbor sites (see Fig. S6a, ESI†). The parameters are fitted with the first-principles band structure within the method of steepest descent, and they are

$$\varepsilon_a = \varepsilon_e = 0.9947\ \text{eV},\ \varepsilon_b = \varepsilon_c = \varepsilon_d = \varepsilon_f = 1.1549\ \text{eV}$$

$$t_1 = -0.870\ \text{eV},\ t_2 = -1.1272\ \text{eV},\ t_3 = 1.0689\ \text{eV},\ t_4 = -0.5641\ \text{eV}$$

The parameters fitted here are based on the two bands of the Dirac cone, and the corresponding result is presented in Fig. S6 (ESI†). Then, we focus on the k_x axis, where the Dirac cone is located. By solving the eigenvalues of the Hamiltonian, we find that the position of the Dirac cone can be shifted along the k_x axis under perturbation in the parameter space.

In addition, based on the above parameters, we have calculated the edge states for the B_6F_2 strip, and there is a clear edge state connected by two Dirac cones (see Fig. S6c, ESI†). As shown in Fig. S3d (ESI†), the in-plane sp^2 hybrid states also contribute partially in the vicinity of the Dirac cone, which can explain the detailed mismatch between the TB model band and first-principles results. Thus, we have calculated the band structure of B_6F_2 by using a tight-binding Hamiltonian with maximally localized Wannier functions[48,49] with the basis sets of sp^2 and p$_z$ orbitals, and the obtained band structures fit well with the GGA-PBE results (see Fig. S6d, ESI†).

Understanding the graphene-like Dirac cones in 2D B structures based on the bond distribution model

The successful application of the 8-electron bond distribution model to the Dirac cones in B_3X (X = H, F, and Cl) urged us to further apply it to understand the previously known Dirac cones of 2D B structures.[23,25,26,50] The 8-electron model stresses that every B atom should satisfy the 8-electron rule based on the summation of the nearest 3c-2e and 2c-2e bonds.[41,43]

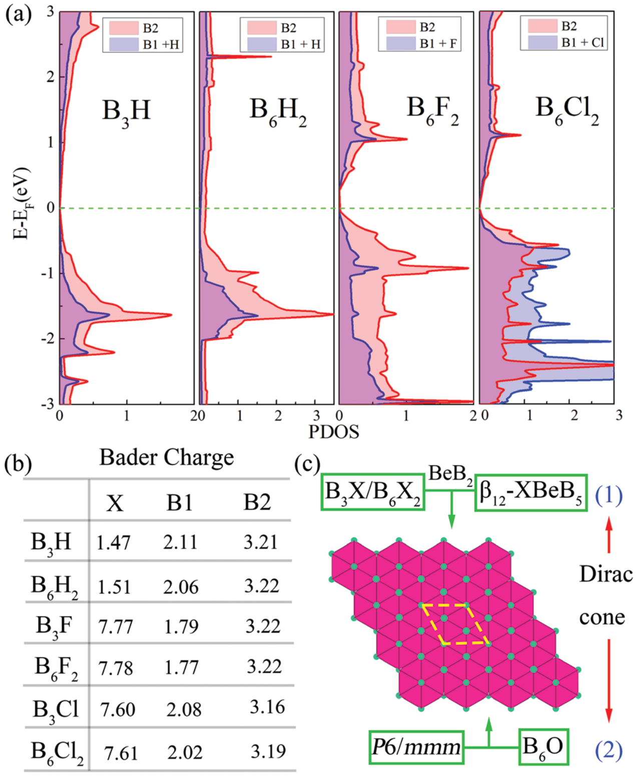

Bader Charge

	X	B1	B2
B_3H	1.47	2.11	3.21
B_6H_2	1.51	2.06	3.22
B_3F	7.77	1.79	3.22
B_6F_2	7.78	1.77	3.22
B_3Cl	7.60	2.08	3.16
B_6Cl_2	7.61	2.02	3.19

Fig. 5 Electronic states and bond model analysis for the new phases. (a) The atomic projected density of states for the phases; B1 represents the B atoms bonded with X, and B2 represents the B atoms at the honeycomb layer. (b) The results of Bader charge analysis for the new phases. The values presented here are the average values of the same types of atoms. (c) The bond model solution for the boron-based Dirac semimetals; the occupation number of the pink triangles (3c-2e bond) is 2/3.

Starting from the triangular B sheet, once the 1 e surplus of the $p(\sqrt{3} \times \sqrt{3})$ triangular B sheet (based on the AEC mechanism) is transferred by the anions, the charge distributions of the B atoms can be described by the simple pattern based on 3c-2e bonds with an occupation of 2/3, such as in B_3X (see Fig. 5c). On the other hand, starting from the honeycomb borophene, the 2 e deficiency in the borophene unit cell can be compensated by charge transfer from metal atoms, such as in BeB_2 monolayer, which is a Dirac semimetal with slight isotropic strains.[23] We note that the B_3X phases (shown in Fig. 1) consist of BB_2 structures and X ligands. If the BB_2 structure donates 1 e to the anion ligand, then it is electronically equivalent to BeB_2. Therefore, the Dirac cones in BeB_2 could also be explained by the 8-electron bond distribution model as in B_3X. Beyond BeB_2, the graphene-like Dirac cone in rectangular β_{12}-$XBeB_5$[50] can also be explained by the model analysis of 3c-2e bonds with the occupation of 2/3. Clearly, the various ligands follow the same rule of ensuring that the 2 e are shared by the honeycomb boron planes, which are equal to the Be atoms in BeB_2 monolayers. Notably, the interlayer B–B bond in the bilayer *P6/mmm* phase[25] and B–O bond in the B_6O sandwich[26] are another effective way to transfer the superfluous 2 e from the two triangular B sheets.[51] Thus, both bilayer *P6/mmm* and the B_6O sandwich share similar double Dirac cone features. Clearly, the Dirac-cones in the above systems are all based on effective charge transfer to form the ideal 3c-2e bond distributions within the constraint of the 8-electron rule. Notably, the 3c-2e bonds are located in the triangular regions in the boron-based nanostructures, which is a unique bonding feature in boron chemistry.[33,52] Thus, the 3c-2e model is proper in boron-based nano-structures due to the electron deficiency, whereas the other honeycomb materials with simple 2c-2e bonds do not need this complicated multicenter bond model.

Due to the flexible bonding configurations between boron and transition metal (TM) atoms, various planar hyper-coordinated species of TM@B_n (n = 7–10) with the TM atom at the center of the boron wheel have been confirmed by experiments.[53,54] Introducing suitable TM atoms to the center of the honeycomb boron network not only can stabilize the planar structures but also may induce novel electronic states. Until now, three TMB_2 (TM = Fe, Ti, or Zr) monolayers have been reported, which are ideal 2D Dirac semimetals with Dirac points near the Fermi level.[20–22] To have a comprehensive comparison of the Dirac cones in B_3X and TMB_2, here, we have calculated the projected band structure for the three TMB_2 phases (see Fig. S7, ESI†). Clearly, the Dirac cones in these systems are dominated by the electronic states from the TM atoms' partially filled *d* orbitals, which are totally different from the ones in B_3X. Although three TMB_2 monolayers share the same symmetry, the locations of the Dirac cones are various, which is due to the different orbital filling. Compared with the Dirac cones in B–X, the counterpart realized in TMB_2 is hard to forecast, which is due to the complicated *d* orbitals of transition metals.

4. Conclusions

In summary, we have designed a family of B_3X (X = H, F, and Cl) 2D materials with graphene-like Dirac cones based on DFT calculations. We have confirmed that the above B_3X systems have high dynamic and thermal stabilities, and they may be synthesized in future experiments. Combined with the projected band structures and TB model analysis, we have illuminated the characteristics of the graphene-like Dirac cones. Furthermore, we have demonstrated that the formation of the Dirac cones can be understood by the AEC mechanism with a bond distribution model, further verified by the Bader charge analysis. We have systematically studied the structural features and internal origin of the 2D boron-based Dirac materials, highlighting that the key mechanism to design the ideal Dirac cones is the optimal orbital filling for the 3c-2e bonds. We are inclined to believe that the synthesis of the predicted structures may enrich the diversity of boron-based 2D materials, and the materials with graphene-like Dirac cones may be used to play a similar role to that of graphene in the near future.

Conflicts of interest

There are no conflicts of interest to declare.

Acknowledgements

This work is supported by the Guangdong Natural Science Funds for Distinguished Young Scholars (No. 2014A030306024, 2017B030306008), National Natural Science Foundations of China (Grant No. 11674148, U1601212, 11774239, and 61827815), National Key R&D Program of China (Grant No. 2016YFB0700700), Shenzhen Science and Technology Innovation Commission (JCYJ20170818093035338, JCYJ20170412110137562, KQTD20170810105439418, KQTD20180412181422399, ZDSYS201707271554071, and ZDSYS20170303165926217), Natural Science Foundation of SZU (Grant No. 827-000242), High-End Researcher Startup Funds of SZU (Grant No. 848-0000040251), and Postdoctoral Science Foundation of China (No. 2019M652996). The computer time at the National Supercomputing Center in Guangzhou (NSCCGZ), Guangzhou Ginpie Technology and the Center for Computational Science and Engineering of Southern University of Science and Technology is gratefully acknowledged.

References

1 G. R. Bhimanapati, Z. Lin, V. Meunier, Y. Jung, J. Cha, S. Das, D. Xiao, Y. Son, M. S. Strano, V. R. Cooper, L. Liang, S. G. Louie, E. Ringe, W. Zhou, S. S. Kim, R. R. Naik, B. G. Sumpter, H. Terrones, F. Xia, Y. Wang, J. Zhu, D. Akinwande, N. Alem, J. A. Schuller, R. E. Schaak, M. Terrones and J. A. Robinson, *ACS Nano*, 2015, **9**, 11509–11539.

2 Y. Zhang, Y.-W. Tan, H. L. Stormer and P. Kim, *Nature*, 2005, **438**, 201–204.

3 M. I. Katsnelson, K. S. Novoselov and A. K. Geim, *Nat. Phys.*, 2006, **2**, 620–625.

4 K. S. Novoselov, A. K. Geim, S. V. Morozov, D. Jiang, M. I. Katsnelson, I. V. Grigorieva, S. V. Dubonos and A. A. Firsov, *Nature*, 2005, **438**, 197–200.

5 J. Wang, S. Deng, Z. Liu and Z. Liu, *Natl. Sci. Rev.*, 2015, **2**, 22–39.

6 A. H. Castro Neto, F. Guinea, N. M. R. Peres, K. S. Novoselov and A. K. Geim, *Rev. Mod. Phys.*, 2009, **81**, 109–162.

7 S. Cahangirov, M. Topsakal, E. Akturk, H. Sahin and S. Ciraci, *Phys. Rev. Lett.*, 2009, **102**, 236804.

8 D. Malko, C. Neiss, F. Vines and A. Goerling, *Phys. Rev. Lett.*, 2012, **108**, 086804.

9 M. Park, Y. Kim and H. Lee, *npj Comput. Mater.*, 2018, **4**, 54.

10 B. Albert and H. Hillebrecht, *Angew. Chem., Int. Ed.*, 2009, **48**, 8640–8668.

11 A. P. Sergeeva, I. A. Popov, Z. A. Piazza, W. L. Li, C. Romanescu, L. S. Wang and A. I. Boldyrev, *Acc. Chem. Res.*, 2014, **47**, 1349–1358.

12 A. J. Mannix, X.-F. Zhou, B. Kiraly, J. D. Wood, D. Alducin, B. D. Myers, X. Liu, B. L. Fisher, U. Santiago, J. R. Guest, M. J. Yacaman, A. Ponce, A. R. Oganov, M. C. Hersam and N. P. Guisinger, *Science*, 2015, **350**, 1513–1516.

13 B. J. Feng, J. Zhang, Q. Zhong, W. B. Li, S. Li, H. Li, P. Cheng, S. Meng, L. Chen and K. H. Wu, *Nat. Chem.*, 2016, **8**, 564–569.

14 S.-G. Xu, X.-T. Li, Y.-J. Zhao, J.-H. Liao, W.-P. Xu, X.-B. Yang and H. Xu, *J. Am. Chem. Soc.*, 2017, **139**, 17233–17236.

15 A. J. Mannix, Z. Zhang, N. P. Guisinger, B. I. Yakobson and M. C. Hersam, *Nat. Nanotechnol.*, 2018, **13**, 444–450.

16 B. Feng, O. Sugino, R.-Y. Liu, J. Zhang, R. Yukawa, M. Kawamura, T. Iimori, H. Kim, Y. Hasegawa, H. Li, L. Chen, K. Wu, H. Kumigashira, F. Komori, T.-C. Chiang, S. Meng and I. Matsuda, *Phys. Rev. Lett.*, 2017, **118**, 096401.

17 H. Zhang, Y. Xie, Z. Zhang, C. Zhong, Y. Li, Z. Chen and Y. Chen, *J. Phys. Chem. Lett.*, 2017, **8**, 1707–1713.

18 B. Feng, J. Zhang, S. Ito, M. Arita, C. Cheng, L. Chen, K. Wu, F. Komori, O. Sugino, K. Miyamoto, T. Okuda, S. Meng and I. Matsuda, *Adv. Mater.*, 2018, **30**, 1704025.

19 S. Gupta, A. Kutana and B. I. Yakobson, *J. Phys. Chem. Lett.*, 2018, **9**, 2757–2762.

20 L. Z. Zhang, Z. F. Wang, S. X. Du, H. J. Gao and F. Liu, *Phys. Rev. B: Condens. Matter Mater. Phys.*, 2014, **90**, 161402.

21 H. Zhang, Y. Li, J. Hou, A. Du and Z. Chen, *Nano Lett.*, 2016, **16**, 6124–6129.

22 A. Lopez-Bezanilla, *Phys. Rev. Mater.*, 2018, **2**, 011002.

23 Y. Mu, F. Ding and H. Lu, *RSC Adv.*, 2015, **5**, 11392–11396.

24 Z. Zhang, E. S. Penev and B. I. Yakobson, *Chem. Soc. Rev.*, 2017, **46**, 6746–6763.

25 F. Ma, Y. Jiao, G. Gao, Y. Gu, A. Bilic, Z. Chen and A. Du, *Nano Lett.*, 2016, **16**, 3022–3028.

26 R. Zhang, Z. Li and J. Yang, *J. Phys. Chem. Lett.*, 2017, **8**, 4347–4353.

27 Z. Zhang, E. S. Penev and B. I. Yakobson, *Nat. Chem.*, 2016, **8**, 525–527.

28 G. Kresse and J. Furthmüller, *Phys. Rev. B: Condens. Matter Mater. Phys.*, 1996, **54**, 11169–11186.

29 G. Kresse and D. Joubert, *Phys. Rev. B: Condens. Matter Mater. Phys.*, 1999, **59**, 1758–1775.

30 J. P. Perdew, K. Burke and M. Ernzerhof, *Phys. Rev. Lett.*, 1996, **77**, 3865–3868.

31 A. Togo, F. Oba and I. Tanaka, *Phys. Rev. B: Condens. Matter Mater. Phys.*, 2008, **78**, 134106.

32 S. Nosé, *J. Chem. Phys.*, 1984, **81**, 511–519.

33 H. Tang and S. Ismail-Beigi, *Phys. Rev. Lett.*, 2007, **99**, 115501.

34 X. Yang, Y. Ding and J. Ni, *Phys. Rev. B: Condens. Matter Mater. Phys.*, 2008, **77**, 041402.

35 W. Li, L. Kong, C. Chen, J. Gou, S. Sheng, W. Zhang, H. Li, L. Chen, P. Cheng and K. Wu, *Sci. Bull.*, 2018, **63**, 282–286.

36 E. S. Penev, S. Bhowmick, A. Sadrzadeh and B. I. Yakobson, *Nano Lett.*, 2012, **12**, 2441–2445.

37 S. N. Shirodkar, E. S. Penev and B. I. Yakobson, *Sci. Bull.*, 2018, **63**, 270–271.

38 Y. Jiao, F. Ma, J. Bell, A. Bilic and A. Du, *Angew. Chem., Int. Ed.*, 2016, **55**, 10292–10295.

39 I. Tateishi, N. T. Cuong, C. A. S. Moura, M. Cameau, R. Ishibiki, A. Fujino, S. Okada, A. Yamamoto, M. Araki, S. Ito, S. Yamamoto, M. Niibe, T. Tokushima, D. E. Weibel, T. Kondo, M. Ogata and I. Matsuda, *Phys. Rev. Mater.*, 2019, **3**, 024004.

40 W. H. Eberhardt, B. Crawford Jr. and W. N. Lipscomb, *J. Chem. Phys.*, 1954, **22**, 989–1001.

41 S.-G. Xu, Y.-J. Zhao, J.-H. Liao and X.-B. Yang, *J. Chem. Phys.*, 2015, **142**, 214307.

42 S.-G. Xu, Y.-J. Zhao, X.-B. Yang and H. Xu, *J. Phys. Chem. C*, 2017, **121**, 11950–11955.

43 S.-G. Xu, X.-T. Li, Y.-J. Zhao, J.-H. Liao, H. Xu and X.-B. Yang, *Nanoscale*, 2018, **10**, 13410–13416.

44 H. Nishino, T. Fujita, N. T. Cuong, S. Tominaka, M. Miyauchi, S. Iimura, A. Hirata, N. Umezawa, S. Okada, E. Nishibori, A. Fujino, T. Fujimori, S.-I. Ito, J. Nakamura, H. Hosono and T. Kondo, *J. Am. Chem. Soc.*, 2017, **139**, 13761–13769.

45 M. Martinez-Canales, T. R. Galeev, A. I. Boldyrev and C. J. Pickard, *Phys. Rev. B*, 2017, **96**, 195442.

46 H. Zabel, *J. Phys.: Condens. Matter*, 2001, **13**, 7679–7690.

47 L. J. Karssemeijer and A. Fasolino, *Surf. Sci.*, 2011, **605**, 1611–1615.

48 N. Marzari, A. A. Mostofi, J. R. Yates, I. Souza and D. Vanderbilt, *Rev. Mod. Phys.*, 2012, **84**, 1419–1475.

49 A. A. Mostofi, J. R. Yates, Y.-S. Lee, I. Souza, D. Vanderbilt and N. Marzari, *Comput. Phys. Commun.*, 2008, **178**, 685–699.

50 J.-H. Yang, S. Song, S. Du, H.-J. Gao and B. I. Yakobson, *J. Phys. Chem. Lett.*, 2017, **8**, 4594–4599.

51 S.-G. Xu, X.-T. Li, Y.-J. Zhao, W.-P. Xu, J.-H. Liao, X.-W. Zhang, H. Xu and X.-B. Yang, *Nanoscale*, 2019, **11**, 7866–7874.

52 A. N. Alexandrova, A. I. Boldyrev, H.-J. Zhai and L.-S. Wang, *Coord. Chem. Rev.*, 2006, **250**, 2811–2866.

53 C. Romanescu, T. R. Galeev, W.-L. Li, A. I. Boldyrev and L.-S. Wang, *Angew. Chem., Int. Ed.*, 2011, **50**, 9334–9337.

54 W.-L. Li, C. Romanescu, T. R. Galeev, Z. A. Piazza, A. I. Boldyrev and L.-S. Wang, *J. Am. Chem. Soc.*, 2012, **134**, 165–168.